

Towards a precision measurement of the Casimir force in a cylinder-plane geometry

M. Brown-Hayes,¹ D.A.R. Dalvit,² F.D. Mazzitelli,³ W.J. Kim,¹ and R. Onofrio^{1,4}

¹*Department of Physics and Astronomy, Dartmouth College, 6127 Wilder Laboratory, Hanover, NH 03755, USA*

²*Theoretical Division, MS B213, Los Alamos National Laboratory, Los Alamos, NM 87545, USA*

³*Departamento de Física J.J. Giambiagi, Facultad de Ciencias Exactas y Naturales,
Universidad de Buenos Aires, Ciudad Universitaria, Pabellon 1, 1428 Buenos Aires, Argentina*

⁴*Dipartimento di Fisica "G. Galilei", Università di Padova, Via Marzolo 8, Padova 35131, Italy*

(Dated: April 5, 2018)

We report on a proposal aimed at measuring the Casimir force in the cylinder-plane configuration. The Casimir force is evaluated including corrections due to finite parallelism, conductivity, and temperature. The range of validity of the proximity force approximation is also discussed. An apparatus to test the feasibility of a precision measurement in this configuration has been developed, and we describe both a procedure to control the parallelism and the results of the electrostatic calibration. Finally we discuss the possibility of measuring the thermal contribution to the Casimir force and deviations from the proximity force approximation, both of which are expected at relatively large distances.

PACS numbers: 12.20.Fv, 03.70.+k, 04.80.Cc, 11.10.Wx

I. INTRODUCTION

The study of quantum vacuum in modern physics is crucial due to its profound implications over a broad range of lengthscales, from elementary particle physics and quantum field theory [1] to cosmology [2, 3, 4, 5, 6]. In between the extremes, the Casimir force [7] has provided an experimentally accessible window at the mesoscopic scale through which significant information about quantum vacuum can be retrieved. The Casimir force, which can be interpreted as the net effect of the radiation pressure resulting from the zero point electromagnetic fluctuations, has been studied in detail both theoretically and experimentally [8, 9, 10, 11, 12, 13, 14, 15]. A first generation of experimental studies immediately followed this prediction, both in the parallel plane configuration originally proposed by Casimir himself [16], and in a variant of this configuration based upon a sphere and a plane [17]. These attempts had partial success in measuring the Casimir force due to a variety of technical issues. In the last decade, a new wave of experiments have succeeded in measuring the force in the parallel plane and in the sphere-plane geometries. The accuracy obtained in the measurements ranges from 15% in the parallel plane case [18] to 0.1-5% in the sphere-plane case [19, 20, 21, 22, 23]. The accuracy for the former configuration is limited mainly by the stringent requirements for parallelism between the two plates while in the latter configuration the limitation is due to the small force signal available, leading to a maximum explorable distance between sphere and plane of about $1\mu\text{m}$ [24]. At distances smaller than $1\mu\text{m}$ the correction to the Casimir force due to finite conductivity and roughness of the substrates cannot be neglected, and has to be taken into account in the theoretical expression of the force. Furthermore, the Casimir force in the sphere-plane configuration is evaluated by using the so-called proximity force approximation

[25, 26], introducing an uncertainty, estimated to be in the 0.1 % range, in the theoretical prediction.

In this paper we report on theoretical and experimental studies of a geometry which interpolates between the two abovementioned configurations, namely the cylinder-plane geometry. This geometry is a compromise between the parallel plane and sphere-plane configurations, as it offers a simpler way to control the parallelism, with respect to the former geometry, while providing a sufficiently increased force signal at large distances in comparison to the sphere-plane configuration. The study of the cylinder-plane configuration also provides insights into the finite temperature contribution to the Casimir force, as well as into the validity of the proximity force approximation. We show how some of these open issues in large-distance Casimir physics, still to be pursued in the laboratory, are easier to deal with in this geometry with respect to those already studied. Mastering the Casimir force at the highest level of accuracy is mandatory to give limits to other macroscopic forces acting in the micrometer range, such as expected corrections to the Newtonian gravitational force [27].

The paper is organized as follows: in Section II we discuss the Casimir force in the cylinder-plane geometry introducing the main sources of deviation from ideality such as finite parallelism, finite conductivity, and finite temperature. Prior to this, the calculation of the electrostatic force in the same geometry is presented. This is crucial not only for the calibration of the apparatus, by applying externally controlled electric fields, but also for the discussion of the expected background noise due to unavoidable residual electrical charges present on the two surfaces. Also, the validity of the proximity force approximation and some related subtleties in its definition at the next-to-leading order are discussed. In Section III, we present an apparatus developed at Dartmouth to test the basic principle of the measurement and to demon-

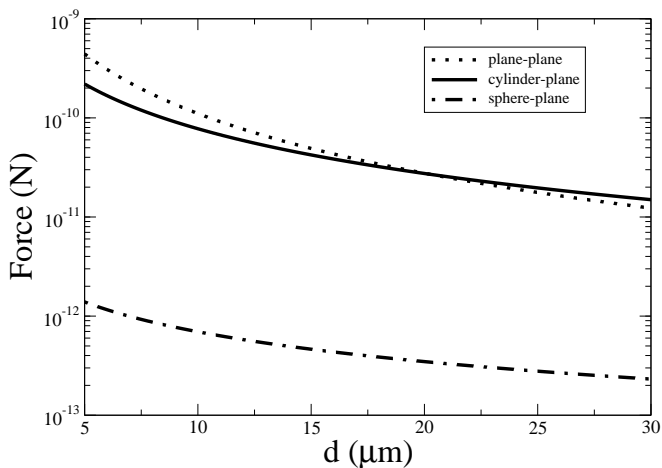


FIG. 1: Absolute electrostatic forces for parallel plane (dotted curve), cylinder-plane (solid), and sphere-plane configurations (dot-dashed). The force in the plane-plane case is given by $F_{\text{El}}^{(0)} = \epsilon_0 AV^2/2d^2$, and in the sphere-plane case it is given by $F_{\text{El}}^{(0)} = 2\pi\epsilon_0 V^2 \sum_{n=1}^{\infty} [\coth(u) - n \coth(nu)] / \sinh(nu)$, with $\cosh(u) = 1 + d/R$. We use $V = 50\text{mV}$ for the bias voltage, $A = 1\text{mm}^2$ for the surface area of the parallel plane configuration, $L = 1\text{cm}$ for the length of the cylinder, $a = 100\mu\text{m}$ for the radius of the cylinder, and $R = 100\mu\text{m}$ for the radius of curvature of the sphere. For the parallel plane and sphere-plane configurations these values are taken from actual experiments described in Refs. [18] and [20], respectively.

strate various techniques specific to this configuration. In Section IV, we present the projected sensitivity of the apparatus. This leads to a discussion of the possible exploratory physics, in particular the measurement of the thermal contribution to the Casimir force and the test of the validity of the proximity force approximation.

II. COULOMB AND CASIMIR FORCES IN A CYLINDER-PLANE GEOMETRY

A. Electrostatic force

A first step towards measuring the Casimir force in the cylinder-plane geometry is to evaluate the force signal expected for the corresponding electrostatic force. Any apparatus for measuring the Casimir force has to be calibrated with a more controllable, better understood, force like the Coulomb force. Additionally, the electrostatic force is unavoidably present as a background due to the residual electric charges on the conducting surfaces. Let us consider a perfectly conducting cylinder of length L and radius a (with $L \gg a$ to neglect border effects) kept at a fixed electrostatic potential V_0 . The cylinder is parallel to a perfectly conducting, grounded, planar surface of area A , and the distance between the two conductors is denoted by d . For this geometry, the exact electrostatic force between the cylinder and the plane is given by [28]

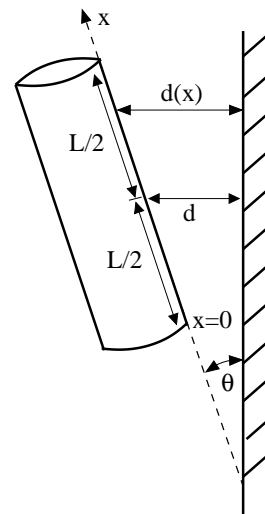


FIG. 2: Geometrical construction of the non-parallel configuration. For the proximity approximation, the local distance between the cylinder and the plane is $d(x) = d - (L/2 - x) \tan \theta$.

$$F_{\text{El-ex}}^{(0)} = \frac{4\pi\epsilon_0 LV_0^2}{\Delta \ln^2 \left(\frac{h-\Delta}{h+\Delta} \right)}, \quad (1)$$

where $\Delta = \sqrt{h^2 - a^2}$ and $h = d + a$. In the limit $d \ll a$, this expression reduces to

$$F_{\text{El}}^{(0)} = \frac{\pi\epsilon_0 \sqrt{a} LV_0^2}{2\sqrt{2} d^{3/2}}. \quad (2)$$

As we will discuss below, this equation can also be derived using the proximity force approximation [25, 26]. In Fig. 1 we compare the absolute electrostatic forces corresponding to the parallel plane, cylinder-plane and sphere-plane configurations with typical values of the relevant parameters, already achieved or achievable in practice. Since, under general experimental conditions, the cylinder and the plane will not be perfectly parallel, we need to calculate the corrections to Eq. (2) due to non-parallelism. This is easily obtained by using the proximity force approximation, with a local distance between the cylinder and the plane given by $d(x) = d - (L/2 - x) \tan \theta$ (see Fig. 2). We obtain

$$\begin{aligned} F_{\text{El}}^{\text{np}} &= F_{\text{El}}^{(0)} \frac{1}{\alpha} \left(\frac{1}{\sqrt{1-\alpha}} - \frac{1}{\sqrt{1+\alpha}} \right) \\ &\approx F_{\text{El}}^{(0)} \left[1 + \frac{5}{8} \alpha^2 + O(\alpha^4) \right], \end{aligned} \quad (3)$$

where $\alpha = L \sin \theta / 2d$. As described in the next section, the quadratic dependence of the electrostatic force on the angle measuring the deviation from the ideal parallelism provides a way to optimize the parallelism between the cylinder and the plane during the electrostatic calibration.

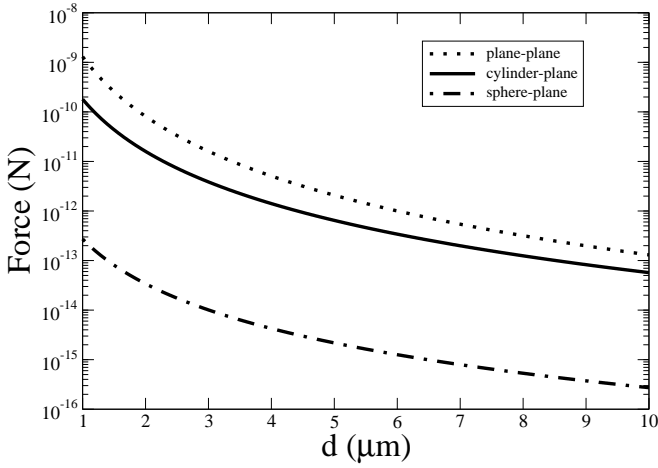


FIG. 3: Absolute Casimir force for plane-plane (dotted curve), cylinder-plane (solid), and sphere-plane configurations (dot-dashed). For the plane-plane case it is given by $F_{\text{Cas}}^{(0)} = \pi^2 \hbar c A / 240 d^4$. The latter two are evaluated within the proximity force approximation. For the sphere-plane case it is given by $F_{\text{Cas}}^{(0)} = \pi^3 \hbar c R / 360 d^3$. Parameters are the same as in Fig. 1.

B. Casimir force

To evaluate the Casimir force between the cylinder and the plane we use once again the proximity force approximation. For the parallel case ($\alpha = 0$), the Casimir force between the cylinder and the plane is attractive, and its magnitude in the limit $d \ll a$ is given by [29]

$$F_{\text{Cas}}^{(0)} = \frac{\pi^3 \hbar c L a^{1/2}}{384 \sqrt{2} d^{7/2}}. \quad (4)$$

The scaling of the Casimir force with distance in the cylinder-plane geometry is intermediate between the sphere-plane case ($\propto d^{-3}$) and the parallel plane configuration ($\propto d^{-4}$). The absolute force signal, for typical values of the relevant parameters, is also intermediate (see Fig. 3). With respect to the sphere-plane geometry, one can enhance the signal by exploiting the linear dimension, *i.e.* the size L , as long as the parallelism between the cylinder and the planar surface does not become an issue. In comparison to the parallel plane situation, in the cylinder-plane configuration one needs to parallelize in only one spatial dimension instead of two, the latter being a considerably more difficult task. The correction to the cylinder-plane Casimir force in the slightly non-parallel case reads

$$F_{\text{Cas}}^{\text{np}} = F_{\text{Cas}}^{(0)} \frac{1}{5\alpha} \left(\frac{1}{\sqrt{(1-\alpha)^5}} - \frac{1}{\sqrt{(1+\alpha)^5}} \right) \approx F_{\text{Cas}}^{(0)} \left[1 + \frac{21}{8} \alpha^2 + O(\alpha^4) \right], \quad (5)$$

which shows a strong similarity to the non-parallel Coulomb force, just differing at the leading orders by the

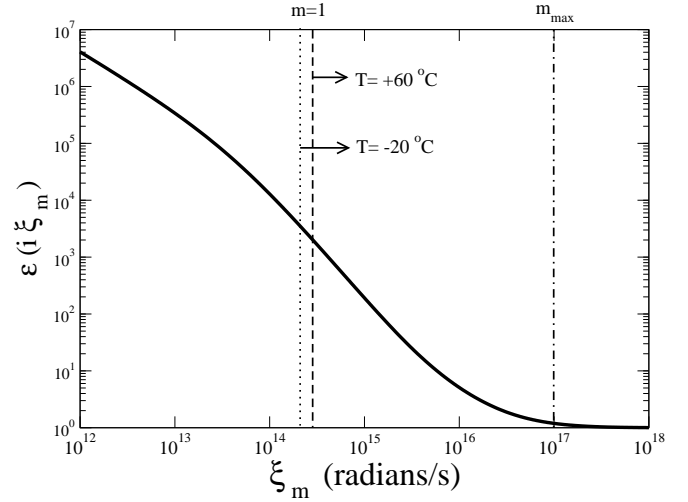


FIG. 4: Permittivity for Au as a function of frequency calculated from optical data (courtesy of Astrid Lambrecht and Serge Reynaud). Permittivity data for Matsubara frequencies with $m \geq 1$ in the range of temperatures of interest $-20^\circ\text{C} \leq T \leq +60^\circ\text{C}$ can be obtained from this plot. The vertical lines show the frequency region used in the m summation over the Matsubara frequencies. The dotted line corresponds to $m = 1$ at $T = -20^\circ\text{C}$, the dashed line to $m = 1$ at $T = +60^\circ\text{C}$, and the dotted-dashed line to the maximum value m_{max} used at all temperatures, corresponding to a maximum Matsubara frequency of $\xi_{\text{max}} = 10^{17}$ rad/s.

coefficient of the quadratic correction in the parameter α .

For an accurate comparison between experiment and theory, apart from the deviations from parallelism already taken into account within the proximity force approximation scheme, we consider the deviations of the predicted force from the ideal situation of perfect conductors, zero roughness, and zero temperature. For typical surfaces and realistic experimental sensitivities, the roughness correction is negligible with respect to other deviations at the distances we are interested in ($d > 1 \mu\text{m}$). On the other hand, combined temperature and conductivity corrections are usually important in this range of distances. We have computed these corrections via the Lifshitz formalism [30], which provides an expression for the pressure between two infinite, parallel plates. We have then used this result in the proximity force approximation for the cylinder-plane configuration. The Casimir pressure in the plane-plane configuration at finite temperature T is given by the Lifshitz formula

$$P(d) = -\frac{1}{\pi \beta d^3} \sum_{m=0}^{\infty} \int_{m\gamma}^{\infty} dy y^2 \times \left[\frac{r_{\text{TM}}^{-2} e^{-2y}}{1 - r_{\text{TM}}^{-2} e^{-2y}} + \frac{r_{\text{TE}}^{-2} e^{-2y}}{1 - r_{\text{TE}}^{-2} e^{-2y}} \right], \quad (6)$$

where d is the gap between the plates, $\beta = 1/k_{\text{B}}T$ is the inverse temperature, and $\gamma = 2\pi d/\beta \hbar c$. The prime

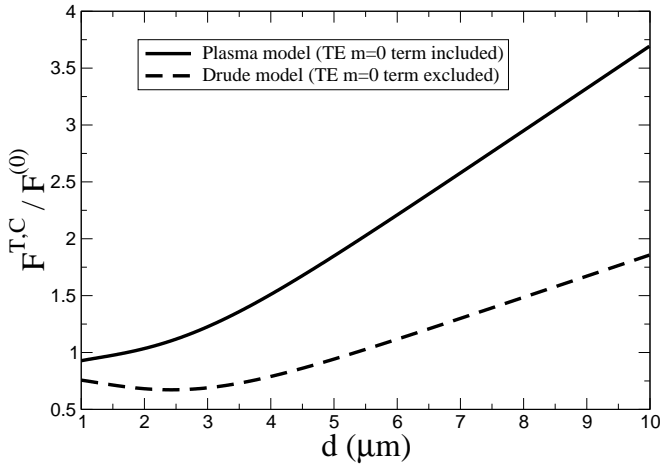


FIG. 5: Combined thermal and conductivity corrections to the Casimir force in the cylinder-plane geometry. We show the Casimir force, normalized to its bare value for infinite conductivity and zero temperature, versus the distance d in the case of gold metallic surfaces at a temperature $T = 300^\circ\text{K}$. Optical data are used to calculate the frequency-dependent permittivity of Au. The $m = 0$ contribution to the Lifshitz formula is computed by extrapolating the optical data to zero frequency using two different theoretical approaches: the plasma model (for which the TE $m = 0$ mode contributes to the force), and the Drude model (for which the TE $m = 0$ mode does not contribute). Parameters are the same as in Fig. 1.

on the summation sign indicates that the $m = 0$ term is counted with half weight. The reflection coefficients r_{TE} and r_{TM} for the two independent polarizations TE and TM are computed at imaginary frequencies $\omega_m = i\xi_m$, where $\xi_m = 2\pi m/\beta\hbar$ are the Matsubara frequencies.

Although the foundations for the Lifshitz formula are well established, the exact expressions for the reflectivity coefficients are not. Following the Lifshitz formalism, the reflection coefficients are expressed in terms of the dielectric permittivity $\epsilon(\omega)$ as

$$r_{\text{TM}}^{-2} = \left[\frac{\epsilon(i\xi_m)p_m + s_m}{\epsilon(i\xi_m)p_m - s_m} \right]^2 ; r_{\text{TE}}^{-2} = \left[\frac{s_m + p_m}{s_m - p_m} \right]^2, \quad (7)$$

where $p_m = y/m\gamma$ and $s_m = \sqrt{\epsilon(i\xi_m) - 1 + p_m^2}$.

Using tabulated optical data for different metals [31], it is possible to compute the dielectric permittivity along the imaginary frequency axis [32]. As an example, we show in Fig. 4 the numerically computed permittivity of Au as a function of frequency. For the computation of the m summation in Eq. (6) we used a cut-off m_{max} corresponding to a Matsubara frequency $\xi_{m_{\text{max}}} = 10^{17}\text{rad/sec}$. For the range of temperatures we are interested in ($-20^\circ\text{C} \leq T \leq +60^\circ\text{C}$), permittivity data for all Matsubara frequencies $\xi_m = 2\pi m/\beta\hbar$ corresponding to $m \geq 1$ can be extracted from the optical data (see Fig. 4). To calculate the $m = 0$ contribution, it is however necessary to extrapolate the available data to zero frequency. This extrapolation has been done in the literature using

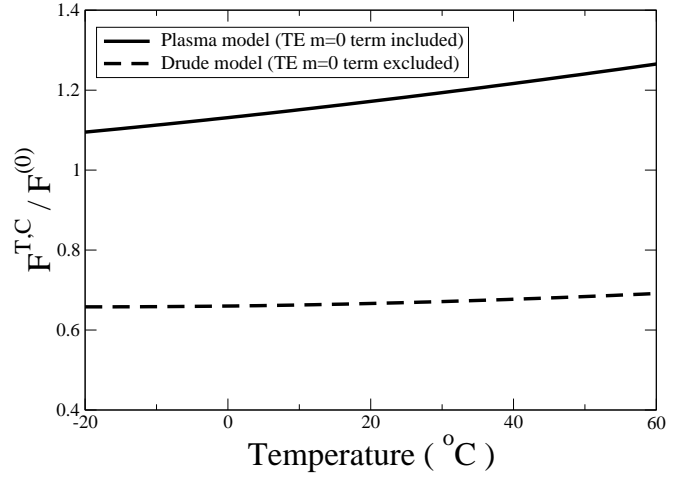


FIG. 6: Dependence upon temperature of the Casimir force in the cylinder-plane geometry. We show the Casimir force, normalized to its bare value for infinite conductivity and zero temperature, versus the temperature T in the case of gold metallic surfaces separated by a distance $d = 3\mu\text{m}$. Extrapolated data for zero frequency ($m = 0$) is obtained from two different theoretical approaches: the plasma model (for which the TE $m = 0$ reflection coefficient is non-zero), and the Drude model (for which the TE $m = 0$ reflection coefficient vanishes). Parameters are the same as in Fig. 1.

different theoretical models, and has led to controversial predictions for the Casimir force between parallel plates [23, 33, 34, 35, 36, 37, 38, 39, 40, 41, 42, 43].

We have computed the Casimir force between the cylinder and the plane using two distinct theoretical approaches. In the first approach, the optical data are extrapolated using the plasma model for the dielectric permittivity [11, 23]: $\epsilon(i\xi) = 1 + \omega_p^2/\xi^2$, where ω_p is the plasma frequency (equal to 9.0 eV for Au). In this model, the reflectivity coefficients for $m = 0$ are given by

$$r_{\text{TM}}^{-2}(m = 0) = 1, \\ r_{\text{TE}}^{-2}(m = 0) = \left[\frac{cy/d + \sqrt{\omega_p^2 + (cy/d)^2}}{cy/d - \sqrt{\omega_p^2 + (cy/d)^2}} \right]^2. \quad (8)$$

In the second approach, we use the model of [43], that extrapolates the optical data using the Drude model: $\epsilon(i\xi) = 1 + \omega_p^2/\xi(\xi + \nu)$, where ν is the relaxation frequency (equal to 35 meV for Au). In this second model, the reflectivity coefficients for $m = 0$ are, in contrast to those found in Eq. (8),

$$r_{\text{TM}}^{-2}(m = 0) = 1 ; r_{\text{TE}}^{-2}(m = 0) = 0. \quad (9)$$

That is, in this second approach the transverse electric zero mode does not contribute to the Casimir force. In Fig. 5 we show the ratio $F_{\text{Cas}}^{T,C}/F^{(0)}$ between the real Casimir force (including temperature and conductivity corrections) and the ideal one (perfect conductors, zero

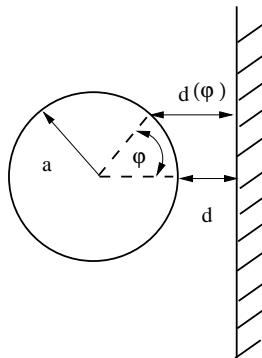


FIG. 7: Cylinder-plane geometry (lateral view). In the proximity force approximation, the force is computed as a superposition of forces between infinitesimal parallel plates, separated by a distance $d(\varphi) = d + a(1 - \cos \varphi)$.

temperature) as a function of the gap d between the cylinder and the plane, assumed to be parallel. The two curves correspond to the two different theoretical approaches described above. As follows from the figure, the ratio of forces increases monotonically with distance for the plasma model, while it shows a small dip close to $3\mu\text{m}$ for the Drude model. In Fig. 6 we show the same ratio of forces as a function of temperature for a fixed gap between the cylinder and the plane, set at $d = 3\mu\text{m}$. The temperature range corresponds to the one we expect to control during the actual Casimir experiment at finite temperature. We see that the normalized force increases with temperature much faster for the plasma model than for the Drude model. In the entire targeted range of temperatures the two models give predicted forces differing by roughly a factor of two, allowing for an easier experimental discrimination, provided that thermal expansion of the materials of the experimental set-up will be kept under control.

C. Accuracy of the proximity force approximation

The calculations of the electrostatic and Casimir forces done in the previous sections rely on the proximity force approximation. We now discuss its validity in the ideal case of zero temperature and perfect conductor.

Let us first consider the proximity force approximation to the electrostatic force in the parallel cylinder-plane configuration

$$F_{\text{El}}^{(i)} = \frac{\epsilon_0 V_0^2}{a^2} \int_0^{\pi/2} \frac{dA_i}{\left(1 + \frac{d}{a} - \cos \varphi\right)^2}. \quad (10)$$

Here dA_i is the effective area of the infinitesimal parts in which the surfaces are divided to integrate the parallel plates result, and φ is the angle parameterizing the location of the infinitesimal surfaces on the cylinder (see Fig. 7). Different choices for this area give distinct proximity approximations for the force [44]. For example, the

area of a small portion of cylinder is $dA_c = Lad\varphi$, while the area of a small portion of plane is $dA_p = La \cos \varphi d\varphi$. One could also use a combination of the two, like the geometric mean $dA_{gm} = (dA_p dA_c)^{1/2}$. These choices for the effective area give the same result to leading order in d/a , but they differ in the subleading corrections

$$\frac{F_{\text{El}}^{(i)}}{F_{\text{El}}^{(0)}} = 1 + \eta_{\text{El}}^{(i)} \frac{d}{a} + O\left(\frac{d^2}{a^2}\right), \quad (11)$$

where $\eta_{\text{El}}^{(p)} = -0.75$, $\eta_{\text{El}}^{(c)} = 0.25$, and $\eta_{\text{El}}^{(gm)} = -0.25$ [45].

One could estimate the error of the proximity force approximation as the difference between these results. However, for the parallel cylinder-plane configuration we know the exact value of the electrostatic force, so we can use it to analyze the accuracy of the different versions of the proximity force approximation. The ratio between the exact and the leading proximity electrostatic forces Eqs. (1) and (2) is given by

$$\frac{F_{\text{El-ex}}^{(0)}}{F_{\text{El}}^{(0)}} = 1 - 0.083 \frac{d}{a} + 0.035 \frac{d^2}{a^2} + \dots \quad (12)$$

Both results coincide within 1% for $d/a < 0.12$.

In Fig. 8 we show the ratios $F_{\text{El}}^{(i)}/F_{\text{El}}^{(0)}$, together with the exact result, also normalized to the leading proximity force approximation in Eq. (2). For small d/a , the exact value of the force is in between $F_{\text{El}}^{(c)}$ and $F_{\text{El}}^{(gm)}$. Moreover, a comparison of Eqs. (11) and (12) shows that the geometric mean prescription is closer to the exact force (a similar result has been obtained for the Casimir interaction energy between concentric cylinders [46]). Had we estimated the error of the proximity force approximation using $F_{\text{El}}^{(c)}$ and $F_{\text{El}}^{(gm)}$, we would have concluded that it is smaller than 1% for $d/a < 0.04$.

For the Casimir case, an analytic expression for the exact force is not available. Therefore, we will estimate the error of the proximity force approximation using $F_{\text{Cas}}^{(c)}$ and $F_{\text{Cas}}^{(gm)}$, defined as

$$F_{\text{Cas}}^{(i)} = \frac{\pi^2 \hbar c}{120a^4} \int_0^{\pi/2} \frac{dA_i}{\left(1 + \frac{d}{a} - \cos \varphi\right)^4}. \quad (13)$$

We obtain

$$\frac{F_{\text{Cas}}^{(i)}}{F_{\text{Cas}}^{(0)}} = 1 + \eta_{\text{Cas}}^{(i)} \frac{d}{a} + O\left(\frac{d^2}{a^2}\right), \quad (14)$$

where $\eta_{\text{Cas}}^{(p)} = -0.15$, $\eta_{\text{Cas}}^{(c)} = 0.05$ and $\eta_{\text{Cas}}^{(gm)} = -0.05$. These results are shown in Fig. 9. We see that, for small d/a , the cylinder-based proximity approximation is larger than the leading order, while the opposite happens for the results based on the plane and on the geometric mean areas. This is analogous to the electrostatic case. Assuming that the exact result is in between $F_{\text{Cas}}^{(c)}$ and $F_{\text{Cas}}^{(gm)}$, we estimate the error of the proximity force as smaller

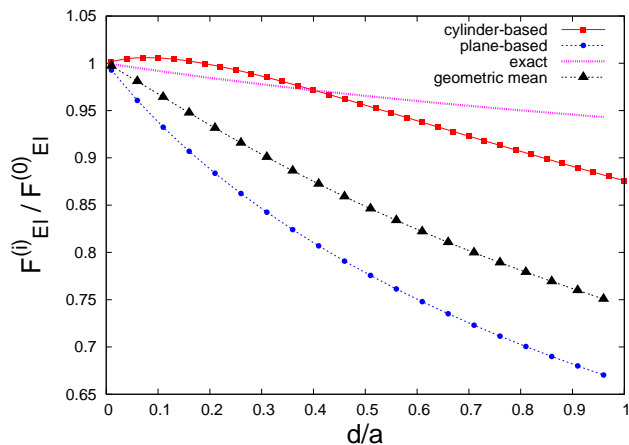


FIG. 8: (Color online) Electrostatic force in the cylinder-plane geometry, normalized to the electrostatic force evaluated in the leading proximity approximation of Eq. (2). We show the exact force (continuous line), and the force evaluated through different proximity approximation schemes obtained using the area of the cylinder (squares), the area of the plane (dots), and a geometric mean of the areas (triangles).

than 1% for $d/a < 0.2$. It is worth to note that the spread of the different approximations is smaller for the Casimir force than for the electrostatic force (see Figs. 8 and 9). This is due to the fact that, as the Casimir force is stronger than the electrostatic one at small distances, the proximity force approximation is dominated by a smaller region around $\varphi = 0$, where the difference between effective area is less important.

The exact Casimir energy for massless scalar fields satisfying Dirichlet boundary conditions in the cylinder-plate geometry has been computed using numerical simulations based on the worldline approach to quantum field theory [47]. Based on an analytic fit of the numerical data [48], we have found a deviation in the force with respect to the leading proximity force of 1% already at $d/a = 0.06$. The difference is about 5% at $d/a = 0.5$. These are still preliminary results, because the precision of the data is not very high, on the order of 10% for small values of d/a [48].

Summarizing, if the Casimir force is measured at the 1% level, in order to see deviations from the proximity force the ratio d/a should be larger than 0.2, according to the estimation based on the different choices of the area. On the other hand, numerical simulations suggest that deviations can already be present at $d/a = 0.06$. Higher precision numerical data for the electromagnetic field are needed to confirm this prediction.

III. ELECTROSTATIC CALIBRATIONS

In order to assess the sensitivity and the requirements for a precision measurement of the Casimir force in a

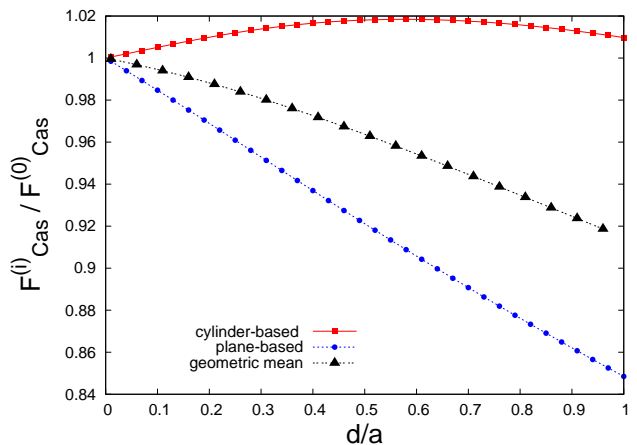


FIG. 9: (Color online) Casimir force in the cylinder-plane geometry, normalized to the Casimir force evaluated in the leading proximity approximation. We show the different proximity approximation schemes obtained using the area of the cylinder (squares), the area of the plane (dots), and a geometric mean of the areas (triangles).

cylinder-plane configuration, we have performed electrostatic calibrations with a prototype of the experimental apparatus (see Fig. 10 for details). The core part of the system is a stainless steel cantilever resonator faced on opposite sides by a stainless steel cylinder and an optical fiber for the detection of its displacement. The resonator is clamped to an aluminum base which is in thermal contact with a thermoelectric cooler for temperature stabilization. Below the resonator is the cylinder, attached to a frame mounted on two piezoelectric actuators providing a maximum displacement of $(15.00 \pm 1.5)\mu\text{m}$ for an applied voltage of 100 V. The two piezoelectric actuators are located along the axis of the cylinder, providing both necessary adjustments for parallelization and the fine approach of the cylinder to the resonator. The coarse approach is provided by a feedthrough micrometer located at the bottom of the vacuum chamber. A few tens of micrometers above the resonator is the optical fiber, which is part of a fiber optic interferometer [49] having as light source a 5 mW diode laser at a wavelength of 671 nm. The displacement signal results from the interference between the light reflected by the resonator and the light internally reflected by the fiber end. The condition of interference which maximizes the displacement sensitivity (obtained at distances for which the dependence of the intensity versus the distance has the maximum slope) is obtained with a coarse approach of the optical fiber to the resonator through a micrometer stage, and a finer tuning with a piezoelectric actuator. The fiber position is stabilized by a servo loop circuit controlling the voltage driving the piezoelectric actuator. The explored resonator-cylinder distances, ranging between 15 μm and 40 μm , are estimated with a digital microscope, allowing for a consistency check with the *a posteriori* de-

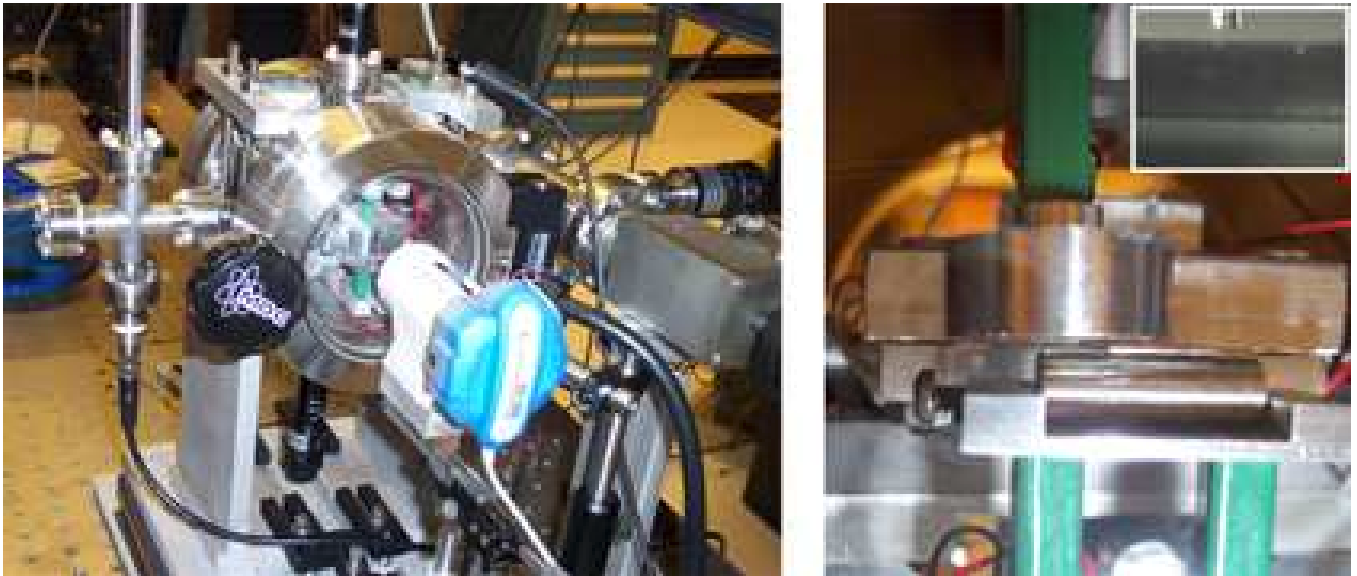


FIG. 10: (Color online) Images of the experimental set-up, with an overall view (left), a close-up on the cylinder-resonator region (right), and an image from the optical microscope (inset). Inside the vacuum chamber are visible the two piezoelectric actuators for the fine approach between the cylinder and the resonator on the bottom side, and the piezoelectric actuator for the fine approach of the optical fiber and its mount on the top side, with the fiber end facing the middle point of the resonator. In between are the resonator and the cylinder, with coarse motion controlled by vertical feedthrough micrometers. The fiber is sent through a feedthrough inside the vacuum chamber (left side in the overall view), while a goniometer stage is used for coarse parallelization (right side in the overall view). The large viewport allows for use of a digital optical microscope with up to $100\times$ magnification for a rough parallelization and a coarse assessment of the fiber-resonator and resonator-cylinder distances, as visible in the inset. The size of the resonator is $2\text{ cm} \times 1\text{ cm} \times 178\text{ }\mu\text{m}$ for width, length, and thickness, respectively. The cylinder has a diameter $2a = 6.35\text{ mm}$ ($1/4\text{ inch}$) and a length of 2 cm .

termination of the gap through data fitting, as described below. Further details on the apparatus setup, its characterization, sensitivity and the noise limitations will be provided in a future publication.

The calibration has been performed by measuring the frequency shift induced by the electrostatic force on the resonator (see for instance [50]). For a generic distance-dependent force (such as the Coulomb force in Eq. (1) or the Casimir force in Eq. (4)), the shift in the proper frequency of the resonator can be written as

$$\Delta\nu^2 = \nu^2 - \nu_0^2 = -\frac{1}{4\pi^2 m} \frac{\partial F(d)}{\partial d}, \quad (15)$$

where m is the effective mass of the mode of oscillation of resonator. The corresponding frequency shift for the Coulomb case then assumes the form

$$\Delta\nu_{\text{El}}^2 = -\frac{3\epsilon_0}{16\sqrt{2}\pi} \frac{\sqrt{a}LV_0^2}{md^{5/2}} = k_c V_0^2, \quad (16)$$

where we have introduced a *curvature* parameter k_c to parameterize the parabolic behavior of $\Delta\nu_{\text{El}}^2$ versus the applied bias voltage V_0 . The determination of the resonant frequency of a mode of oscillation of the cantilever is obtained by driving its motion with a piezoelectric actuator clamped in the proximity of its base and fed by the white noise source of a FFT spectrum analyzer. This last is used to acquire and perform the spectral analysis

of the signal coming from the photodiode collecting the interference light at one port of the fiber mixer.

The electrostatic calibrations can be divided into three steps: a) determination of the parallel configuration by looking at the minimum frequency shift at constant average distance and various tilting angles between the resonator and the cylinder, b) measurements of the frequency shift versus bias voltage in the parallel configuration, and c) repetition of the previous measurements for various values of the cylinder-resonator distance.

In order to determine the parallel configuration, we use the result obtained in Eq. (3), according to which the force exerted on the cantilever is expected to have a parabolic dependence on the angle describing the deviation from the ideal parallelism for small angles θ . The coarse control of the parallelism is obtained by using a goniometer stage on which the resonator is mounted, which can be manually controlled with an in-vacuum feedthrough. For the fine control, two piezoelectric actuators are used in a differential mode, in such a way that the median distance between the resonator and the cylinder (i.e. the distance d between the midpoints of the two structures, see Fig. 2) is unchanged. This is obtained by pivoting the cylinder around the middle point, i.e. by summing and subtracting equal amounts of voltage supplied to the two piezoelectric actuators moving the cylinder position. The plot of the resonator frequency

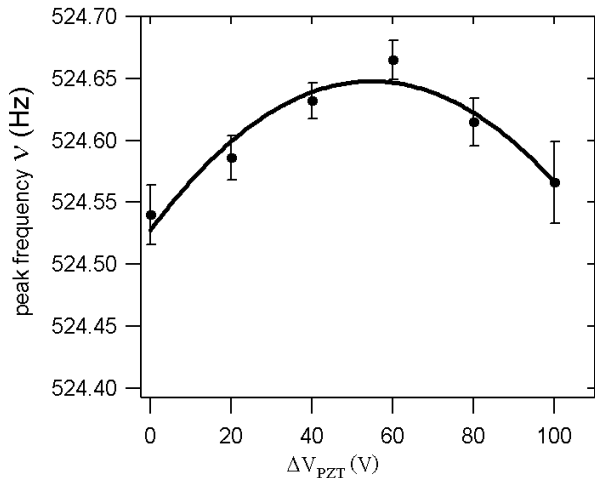


FIG. 11: Assessment of the parallelism. Resonator frequency versus the difference between the voltages applied to the two piezoelectric actuators driving the cylinder base $\Delta V_{\text{PZT}} = V_L - V_R$, starting from a common mode of $V_L = V_R = 50$ V, for $V_0 = 100$ V. The resonator frequency without bias voltage is $\nu_0 = (527.30 \pm 0.02)$ Hz. The maximum frequency (corresponding to the minimum frequency shift with respect to ν_0) realizes the condition for parallelism, and this occurs at $\Delta V_{\text{PZT}} = (54.8 \pm 7.1)$ V. As the two piezoelectric actuators are spaced by 2 cm, this corresponds to achieving parallelism within $\delta\theta = 5.3 \times 10^{-5}$ radians. The determination of the frequency is based upon a fit of the mechanical transfer function of the resonator with a Lorentzian function, obtained through 100 averages of the FFT with a frequency span of 12.5 Hz.

versus the difference between the voltages applied to the left and right piezoelectric actuators acting on the cylinder, for a constant bias voltage difference, has a parabolic dependence for small deviations from parallelism, with its maximum corresponding to the parallel case $\alpha = 0$. The outcome of this procedure is summarized in Fig. 11, where the frequency of the resonator displays a parabolic dependence as a function of ΔV_{PZT} , which reflects different tilting angles θ . The maximum frequency defines the parallelism condition, within the error, which leads to a precision of $\delta\theta = 5.3 \times 10^{-5}$ radians. This corresponds, based on Eq. (5), to a correction equal to $(F_{\text{Cas}}^{\text{np}} - F_{\text{Cas}}^{(0)})/F_{\text{Cas}}^{(0)} = 1.43 \times 10^{-4}$. Notice that, unlike the parallel plane configuration, the search for the parallel situation is considerably simpler and faster to implement in the cylinder-plane geometry as it requires only a one-dimensional optimization [51].

After this preparatory measurement, we have then obtained the frequency shift versus the bias voltage, and the related curvature parameter k_c of the expected parabolic dependence, as shown in Fig. 12. This has been repeated for various distances between the resonator and the cylinder, adding a common mode voltage to the actuators, thereby inducing a global approach of the cylinder to the resonator. In Fig. 13 the curvature parameter k_c is plotted versus the piezoelectric actuator volt-

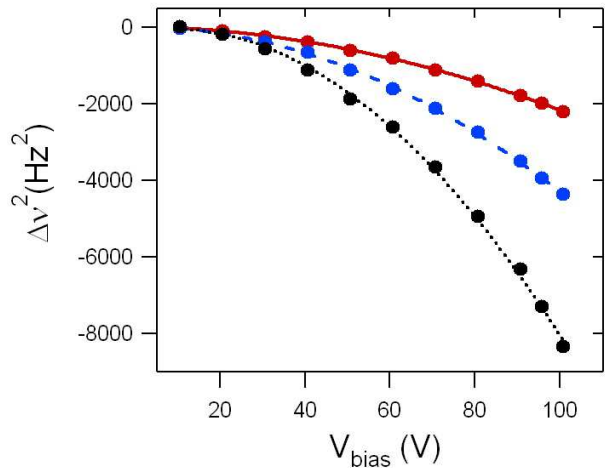


FIG. 12: (Color online) Electrostatic calibrations. Squared frequency shift $\Delta\nu^2$ versus bias voltage between the cylinder and the resonator for different values of the cylinder-plane distance, corresponding to the application of $V_{\text{PZT}} = 0$ V (continuous line), 30 V (dashed line), and 70 V (dotted line). The curves are the best fit with a generic parabola. The typical resonance frequency without bias potential is around 527 Hz, with a bandwidth of 4 Hz. The peak frequency is determined through the Lorentzian fit with a typical error of 12 mHz.

age V_{PZT} . The latter quantity is related to the absolute distance between the cylinder and the resonator as $d = d_{\text{in}} - \alpha_{\text{act}} V_{\text{PZT}}$, where $\alpha_{\text{act}} = (150.0 \pm 15.0) \text{ nm/V}$ is the actuation coefficient of the piezoelectric and d_{in} the initial distance corresponding to $V_{\text{PZT}} = 0$. This allows comparison of the data to the predictions from Eq. (16) of a power-law dependence with scaling $-5/2$ upon the absolute distance. As usually done in this type of measurement, the absolute initial distance has been determined by considering an offset as a free parameter in the fit. A zero distance, shorting the cylinder-plane gap, is reached when the piezoelectric actuator voltage is $V_{\text{PZT}} = d_{\text{in}}/\alpha_{\text{act}} = V_{\text{MAX}}$. From the value of V_{MAX} determined from the fit, $V_{\text{MAX}} = (177.4 \pm 24.1) \text{ V}$, we deduce an initial distance $d_{\text{in}} = \alpha_{\text{act}} V_{\text{MAX}} = (26.6 \pm 4.5) \mu\text{m}$. The estimated minimum gap corresponding to the maximum excursion of the piezoelectric actuator before shorting the gap is therefore $\simeq 16.1 \mu\text{m}$, consistent with the expected roughness of both cylinder and resonator surfaces. The relative accuracy in the determination of the absolute distance in these preliminary calibrations is 17%. Better precision can be obtained by looking at gaps in the 10-30 μm range using a large magnification, high resolution optical microscope. The absolute gap can be accurately determined due to a particular feature of the cylinder-plane configuration: by properly illuminating the gap, the cylinder will appear reflected on the planar surface, and the distance between the cylinder edge and its mirror image on the plane surface can then be measured. Extension of the calibration into the range of interest for the measurement of the Casimir force (1-5 μm) will require

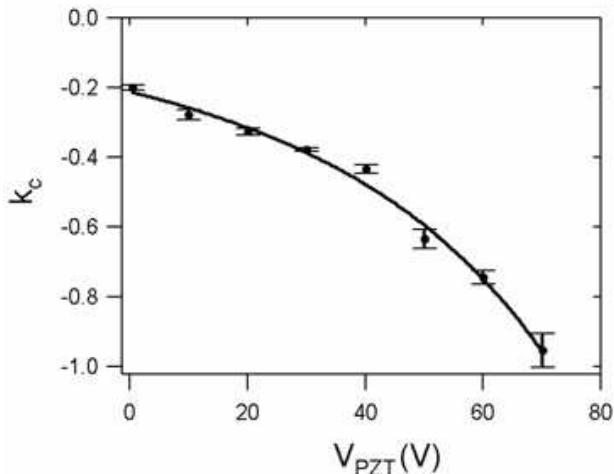


FIG. 13: Electrostatic calibrations. Plot of the curvature coefficient k_c versus the piezoelectric common voltage V_{PZT} and best fit with a law $\Delta\nu^2 = a + b/(V_{MAX} - V_{PZT})^{2.5}$ corresponding to the expected frequency-shift dependence from Eq. (16). The best fit gives a parameter $V_{MAX} = (177.4 \pm 24.1)V$, corresponding to the voltage which should close the gap between the cylinder and the resonator.

high precision nanopositioners with minimal hysteresis, thereby reducing the relative error in the determination of the distance to less than 1%.

IV. EXPECTED CASIMIR FORCE SIGNAL

Based on the electrostatic calibrations and the possible short-term improvements, we now evaluate the sensitivity to physics related to the Casimir effect, in particular the thermal contribution and the test of the validity of the proximity force approximation scheme. The expected frequency shift due to the Casimir force is written as

$$\Delta\nu_{Cas-cp}^2 = -\frac{7\pi}{3072\sqrt{2}} \frac{\hbar c L \sqrt{a}}{m d^{9/2}}. \quad (17)$$

It is worth comparing the expected frequency-shift signal to the one already measured in Padova [18]. The squared frequency shift for a parallel plane configuration is expressed as

$$\Delta\nu_{Cas-pp}^2 = -\frac{\hbar c}{240} \frac{A}{m d^5}, \quad (18)$$

where A is the surface area of the plates. Considering resonators with the same mass for the two configurations corresponding to Eqs. (19) and (20), we obtain a ratio between the expected squared frequency shifts as:

$$\frac{\Delta\nu_{Cas-cp}^2}{\Delta\nu_{Cas-pp}^2} = \frac{35\pi}{64\sqrt{2}} \frac{L\sqrt{ad}}{A}. \quad (19)$$

Apart from a numerical factor of order unity, the ratio between the expected squared frequency shifts is the ratio between the relevant geometrical scales in the two configurations, *i.e.* the transversal size of the resonator-cylinder region L , the geometrical average of the radius of curvature of the cylinder a and the cylinder-plane distance d , and the plates surface area A . By inserting the respective values from the Padova experiment, and a radius of the cylinder of 51 cm (using commercially available cylindrical lenses with proper metallic coating), at the distance $d = 1\mu\text{m}$ the ratio gives $\Delta\nu_{Cas-cp}^2/\Delta\nu_{Cas-pp}^2 \simeq 0.727$. This implies that a frequency shift equal to $\Delta\nu_{cp} = \Delta\nu_{cp}^2/2\nu_0 = 4.08$ mHz (571 mHz) at a gap of $3\mu\text{m}$ ($1\mu\text{m}$) is expected for the cylinder-plane case, as compared to a $\Delta\nu_{pp} = 3.2$ mHz (780 mHz) at a gap of $3\mu\text{m}$ ($1\mu\text{m}$) for the parallel plane case. In preliminary long time average tests with our prototype we have obtained an error on the determination of the peak frequency of the resonator through a Lorentzian fit of $\simeq 6$ mHz. We find that the minimum detectable frequency shift can be made significantly smaller through a careful study of the resonance curve of the mechanical transfer function of the cantilever in a relatively large range of frequencies, equal to 10-20 times its intrinsic bandwidth. A careful fitting of data, with a long sampling time and a large number of averages, allow for the determination of the resonance frequency with a precision of the order of mHz or less, even when working with relatively large mechanical bandwidths as in the case of stainless steel resonators. From this point of view the use of resonators with a large quality factor may not seem advantageous; in order to acquire a resonance curve with the same resolution one needs to adapt a smaller frequency binning resulting in a much longer integration time, which is more vulnerable to frequency shifts possibly induced by the finite degree of stabilization of the temperature of the apparatus. Further improvements in the sensitivity are expected by implementing frequency and amplitude stabilization of the diode laser, high-performance actuators with minimal hysteresis and better displacement resolution, and a better control of the temperature setting and stabilization both for the resonator and for the fiber set-up. Alternative detection schemes, like homodyne or heterodyne modulations [50], may be utilized to improve the precision.

As a final assessment of the experimental set-up, apart from the need for improved planarity and decreased roughness of the resonator and cylinder surfaces using optical quality surfaces, and a careful determination of the absolute distance between the cylinder and the resonator as discussed above, we need to explore the Volta and patch electrostatic potentials present between the two surfaces. To quantify this source of noise it is worth introducing, in analogy to the discussion in [52] for the parallel plane case, the equivalent voltage corresponding, at a given distance, to the Casimir force. By equating

Eqs. (2) and (4) we obtain an equivalent voltage as

$$V_{\text{eq}} = \left(\frac{\pi^2 \hbar c}{192 \epsilon_0} \right)^{1/2} \frac{1}{d} = 13.55 \left(\frac{\mu\text{m}}{d} \right) \text{ mV}. \quad (20)$$

For instance, at a targeted gap of $d = 3\mu\text{m}$ the Casimir force corresponds to an equivalent voltage $V_{\text{eq}} = 4.61$ mV, which implies that one should control the electrostatic stray potentials within a fraction of this value in order to see the thermal contribution to the Casimir force. The capability of counterbiasing the electrostatic potential difference at this level will require a dedicated study in a concrete setting once the gap distances will be reduced to few micrometers. From this point of view it is encouraging that, as visible in Fig. 1, the electrostatic force in the cylinder-plane configuration can exceed at large distances the corresponding one for the parallel plane situation. This can lead to larger signals in a wider range of distances and consequently to a more precise determination of the stray voltages to be counterbiased.

The apparatus could also be adapted to the study of the validity of the proximity force approximation. As we already mentioned at the end of Section II, recent numerical results based on the worldline approach [48] indicate that deviations from the proximity force approximation should be relevant starting from a ratio $d/a \simeq 0.06$ upward. For instance, at a distance of $5\mu\text{m}$ they should be of the order of 1 % for a choice of the radius of the cylinder $a=100\mu\text{m}$. This suggests the use of metallic wires to intentionally look for the deviation from the predictions of the proximity force approximation [47, 48].

V. CONCLUSIONS

We have discussed a novel geometry to study the Casimir force which more adequately addresses current issues related to the large distance behavior of quantum

vacuum fluctuations. In particular, this should allow for the study of the interplay of zero-point fluctuations with the thermal contribution due to the real photons present at any finite temperature. From this point of view the theoretical discussion presented here is complementary to the one presented in [29] for the case of eccentric cylinders, the latter being promising for investigating extra-gravitational forces due to a smaller sensitivity to long-range Casimir related effects. An apparatus to demonstrate some of the concepts developed in this discussion has been built and tested, showing promising features towards the observation of the thermal effect. With an upgraded version of the apparatus, including better thermal stabilization, high precision actuators, and mechanical resonators with decreased roughness, and with a careful study of the stray electrostatic potentials, we should be able to explore the Casimir force in the target range centered around $3\mu\text{m}$ with a precision of a few percent. Moreover, the possible observation of deviations from the force predicted by the proximity force approximation will be important to assess the limits to extra-dimensional forces of gravitational origin.

Acknowledgments

We are grateful to Astrid Lambrecht and Serge Reynaud for providing us with the permittivity data for different metals. We also thank Scott M. Middleman for experimental assistance, Richard L. Johnson for skillful technical support, and Holger Gies for fruitful discussions and for sharing crucial information on worldline numerical simulations prior to publication. M.B.H. acknowledges support from the Dartmouth Graduate Fellowship program, W.J.K. acknowledges the Gordon Hull Fellowship, and F.D.M. acknowledges support from Universidad de Buenos Aires, CONICET and ANPCyT.

-
- [1] P. Milonni, *The Quantum Vacuum* (Academic Press, San Diego, 1994).
 - [2] Y. B. Zeldovich, *Sov. Phys. JETP* **6**, 316 (1967).
 - [3] S. Weinberg, *Rev. Mod. Phys.* **61**, 1 (1989).
 - [4] S. M. Carroll, *Living Rev. Rel.* **4**, 1 (2001).
 - [5] V. Sahni and A. A. Starobinsky, *Int. J. Mod. Phys. D* **9**, 373 (2000).
 - [6] P.J.E. Peebles, *Rev. Mod. Phys.* **75**, 559 (2003).
 - [7] H.B.G. Casimir, *Proc. K. Ned. Akad. Wet. B* **51**, 793 (1948).
 - [8] G. Plunien, B. Müller, and W. Greiner, *Phys. Rep.* **134**, 87 (1986).
 - [9] V. M. Mostepanenko and N. N. Trunov, *The Casimir Effect and its Applications* (Clarendon, London, 1997)
 - [10] M. Bordag, *The Casimir Effect 50 Years Later* (World Scientific, Singapore, 1999).
 - [11] M. Bordag, U. Mohideen, and V. M. Mostepanenko, *Phys. Rep.* **353**, 1 (2001).
 - [12] S. Reynaud, A. Lambrecht, C. Genet, M.T. Jaekel, C. R. Acad. Sci. Paris **IV-2**, 1287 (2001).
 - [13] K. A. Milton, *The Casimir Effect: Physical Manifestations of the Zero-Point Energy* (World Scientific, Singapore, 2001).
 - [14] K. A. Milton, *J. Phys. A: Math. Gen.* **37**, R209 (2004).
 - [15] S.K. Lamoreaux, *Rep. Prog. Phys.* **68**, 201 (2005).
 - [16] M.J. Sparnaay, *Physica* **24**, 751 (1958).
 - [17] P.H.G.M. van Blokland and J.T.G. Overbeek, *J. Chem. Soc. Faraday Trans. I*, **74**, 2637 (1978).
 - [18] G. Bressi, G. Carugno, R. Onofrio, and G. Ruoso, *Phys. Rev. Lett.* **88**, 041804 (2002).
 - [19] S.K. Lamoreaux, *Phys. Rev. Lett.* **78**, 5 (1997).
 - [20] U. Mohideen and A. Roy, *Phys. Rev. Lett.* **81**, 4549 (1998); B.W. Harris, F. Chen, and U. Mohideen, *Phys. Rev. A* **62**, 052109 (2000).
 - [21] H.B. Chan, V.A. Aksyuk, R.N. Kleiman, D.J. Bishop, and F. Capasso, *Science* **291**, 1941 (2001); H. B. Chan,

- V.A. Aksyuk, R.N. Kleiman, D.J. Bishop, and F. Capasso, Phys. Rev. Lett. **87**, 211801 (2001); D. Iannuzzi, I. Gelfand, M. Lisanti, and F. Capasso, Proc. Nat. Ac. Sci. USA **101**, 4019 (2004).
- [22] R.S. Decca, D. Lopez, E. Fischbach, and D.E. Krause, Phys. Rev. Lett. **91**, 050402 (2003); R.S. Decca *et al.*, Phys. Rev. Lett. **94**, 240401 (2005).
- [23] R.S. Decca, D. Lopez, E. Fischbach, G. L. Klimchitskaya, D.E. Krause, and V.M. Mostepanenko, Annals of Physics **318**, 37 (2005).
- [24] In the only sphere-plane experiment exploring distances larger than $1\mu\text{m}$ [19], accuracy at the level of 5 – 10% at the largest explored distances was reported, see A. Lambrecht and S. Reynaud, Phys. Rev. Lett. **84**, 5672 (2000); S.K. Lamoreaux, Phys. Rev. Lett. **84**, 5673 (2000). Also, common to all experiments is the issue of the precision obtainable in the measurement of the absolute value of the distance between the two objects, as further discussed in Section III.
- [25] B. V. Derjaguin and I. I. Abrikosova, Sov. Phys. JETP **3**, 819 (1957); B. V. Derjaguin, Sci. Am. **203**, 47 (1960).
- [26] J. Blocki, J. Randrup, W.J. Swiatecki, and F. Tsang, Ann. Phys. **105**, 427 (1977).
- [27] E. Fischbach and C. L. Talmadge, *The Search for Non-Newtonian Gravity* (AIP/Springer-Verlag, New York, 1999).
- [28] W.R. Smythe, *Static and Dynamic Electricity* (McGraw-Hill, New York, 1968), p. 78.
- [29] D.A.R. Dalvit, F.C. Lombardo, F.D. Mazzitelli, and R. Onofrio, Europhys. Lett. **67**, 517 (2004).
- [30] E.M. Lifshitz, Zh. Eksp. Teor. Fiz **29**, 94 (1956) [Sov. Phys. JETP **2**, 73 (1956)]; E.M. Lifshitz and L.P. Pitaevskii, Statistical Physics, Part 2 (Butterworth-Heinemann, Oxford, 2002).
- [31] Handbook of Optical Constants of Solids (Ed. E. D. Palik, Academic Press, London, 1985).
- [32] A. Lambrecht and S. Reynaud, Eur. Phys. J. D **8**, 309 (2000).
- [33] M. Bostrom and B. E. Sernelius, Phys. Rev. Lett. **84**, 4757 (2000).
- [34] S. K. Lamoreaux, Phys. Rev. Lett. **87**, 139101 (2001); B. E. Sernelius, Phys. Rev. Lett. **87**, 139102 (2001).
- [35] F. Chen, G. L. Klimchitskaya, U. Mohideen, and V. M. Mostepanenko, Phys. Rev. Lett. **90**, 160404 (2003).
- [36] B. Geyer, G. L. Klimchitskaya, and V.M. Mostepanenko, Phys. Rev. A **67**, 062102 (2003); *ibid.* **65**, 062109 (2002).
- [37] R. Esquivel, C. Villarreal, and W.L. Mochan, Phys. Rev. A **68**, 052103 (2003).
- [38] C. Genet, A. Lambrecht, and S. Reynaud, Int. J. Mod. Phys. A **17**, 761 (2002); Phys. Rev. A **62**, 012110 (2000).
- [39] V. B. Svetovoy and M. V. Lokhanin, Phys. Rev. A **67**, 022113 (2003).
- [40] J. R. Torgerson and S. K. Lamoreaux, Phys. Rev. E **70**, 047102 (2004).
- [41] R. Esquivel and V. B. Svetovoy, Phys. Rev. A **69**, 062102 (2004).
- [42] M. Bordag, B. Geyer, G.L. Klimchitskaya, and V.M. Mostepanenko, Phys. Rev. Lett. **85**, 503 (2000).
- [43] J. S. Høye, I. Brevik, J. B. Aarseth, and K. A. Milton, Phys. Rev. E **67**, 056116 (2003); I. Brevik, J. B. Aarseth, J. S. Høye, and K. A. Milton, Phys. Rev. E **71**, 056101 (2005); V. S. Bentsen, R. Herikstad, S. Skriudalen, I. Brevik, and J. S. Høye, quant-ph/0505136.
- [44] One could also consider a proximity force approximation in which the infinitesimal surfaces on the plane and on the cylinder, to which the parallel plane result is applied, are not the closest ones, rather the pair of surfaces connected by the normal to the cylinder. The former are separated by $d(\varphi)/\cos\varphi$. In this approximation there is an additional factor $\cos^2\varphi$ in the proximity integral of Eq. (10).
- [45] The leading and next-to-leading corrections are independent of the upper limit of integration in Eq. (10), because for small d/a the main contribution to the integral comes from the region $\varphi \leq 1$.
- [46] F. D. Mazzitelli, M. J. Sanchez, N. N. Scoccola, and J. von Stecher, Phys. Rev. A **67**, 013807 (2003).
- [47] H. Gies, K. Langfeld, and L. Moyaerts, J. High Energy Phys. **6**, 18 (2003).
- [48] H. Gies, private communication.
- [49] D. Rugar, H. J. Marmin, and P. Guethner, Appl. Phys. Lett. **55**, 2588 (1989).
- [50] G. Bressi, G. Carugno, A. Galvani, R. Onofrio, G. Ruoso, and F. Veronese, Class. Quantum Grav. **18**, 3943 (2001).
- [51] In the parallel plane configuration studied in [18], parallelism was achieved through a complex system of relative micropositioning of the two plates, and monitoring their capacitance with an AC bridge. Micrometer size dust particles in between the plates often resulted in minimum achievable gaps of the order of $3-5\mu\text{m}$, a problem already experienced in [16]. From this point of view a cylinder-plane configuration is more immune to the presence of dust particles, unless they are exactly located along the line of minimum distance between the cylinder and the plane.
- [52] R. Onofrio and G. Carugno, Phys. Lett. A **198**, 365 (1995).